Molecular design of self-coacervation phenomena in block polyampholytes

Scott P. O. Danielsen[a,b], James McCarty[b,c], Joan-Emma Shea[b,c,d], Kris T. Delaney[b,1], and Glenn H. Fredrickson[a,b,e,1]

[a]Department of Chemical Engineering, University of California, Santa Barbara, CA 93106; [b]Materials Research Laboratory, University of California, Santa Barbara, CA 93106; [c]Department of Chemistry and Biochemistry, University of California, Santa Barbara, CA 93106; [d]Department of Physics, University of California, Santa Barbara, CA 93106; and [e]Materials Department, University of California, Santa Barbara, CA 93106

Edited by Pablo G. Debenedetti, Princeton University, Princeton, NJ, and approved March 12, 2019 (received for review January 12, 2019)

Coacervation is a common phenomenon in natural polymers and has been applied to synthetic materials systems for coatings, adhesives, and encapsulants. Single-component coacervates are formed when block polyampholytes exhibit self-coacervation, phase separating into a dense liquid coacervate phase rich in the polyampholyte coexisting with a dilute supernatant phase, a process implicated in the liquid–liquid phase separation of intrinsically disordered proteins. Using fully fluctuating field-theoretic simulations using complex Langevin sampling and complementary molecular-dynamics simulations, we develop molecular design principles to connect the sequenced charge pattern of a polyampholyte with its self-coacervation behavior in solution. In particular, the lengthscale of charged blocks and number of connections between oppositely charged blocks are shown to have a dramatic effect on the tendency to phase separate and on the accessible chain conformations. The field and particle-based simulation results are compared with analytical predictions from the random phase approximation (RPA) and postulated scaling relationships. The qualitative trends are mostly captured by the RPA, but the approximation fails catastrophically at low concentration.

coacervation | polyampholyte | sequence | chain conformation

Polyampholytes are charged copolymers containing positive, negative, and neutral segments. The sequence of those segments can be annealed (i.e., depend on the pH of solution in the case of weak polyampholytes) or quenched randomly or in a specific charge pattern (e.g., alternating or blocky). Polyampholytes exbibit richer phase behavior and chain conformations than polyelectrolytes, their uniformly charged analogues, due to the repulsion between like-charged segments stretching the chain and the attraction between oppositely charged segments collapsing the chain (1–7).

Block polyampholytes, in particular, are an attractive system to study the conformational regimes (8–10) and phase separation (11–14) at different ionic strengths as a function of polyampholyte concentration, fractional charge, net charge, and sequence pattern. The molecular design principles developed should give insight into the more complicated sequences of intrinsically disordered proteins (IDPs) (1, 15–19) and solution environments in vivo affecting the liquid–liquid phase separation responsible for membraneless organelles (20–30).

The liquid–liquid phase separation of block polyampholytes into a polymer-rich phase and a dilute supernatant coexisting primarily of small salt ions is an example of single-component coacervation or self-coacervation. This self-coacervation phenomenon is strikingly similar to the complex coacervation of oppositely charged polyelectrolytes, due to the tendency for polyelectrolytes to form charge-neutral dimers in dilute solution (8, 31). Polyampholytes, however, have chain conformations and phase behavior that are sensitive not only to their total charge, but also to the patterning of charges along the polymer, where self-coacervation is suppressed in charge-scrambled analogues (24, 32). Simple analytical theories based on the random phase approximation (RPA) have partially accounted for the phase behavior of sequence-specific electrostatic interactions for a few specific IDP charge patterns (12–14) and other simple patterns (6, 7, 33), although the RPA is known to break down at low concentration, so it is unable to reliably predict the dilute branch of polyampholyte-phase diagrams. It should also be noted that the widely applied Voorn–Overbeek model of coacervation (34) neglects the connectivity of charges to the polymeric backbone (31, 35, 36) and thus is not useful for understanding sequence-dependent self-coacervation phenomena.

The phase behavior and chain conformations of nearly charge-neutral alternating, random, and diblock polyampholytes have been studied extensively through scaling arguments, RPA, as well as molecular simulations highlighting the attractive electrostatic fluctuations that cause collapse into globular configurations and phase separation at low concentrations (1, 5–9, 19, 33, 37, 38). These approaches have qualitatively matched experiments on synthetic polyampholytes where the overall charge and sequence of charges are difficult to control (3, 4, 39–42), so the accuracy of these approaches is yet unknown. So far, however, the only approximation-free phase diagrams revealing both dilute and concentrated branches of the two-phase coexistence envelopes for polyampholytes in solution have been developed for the symmetric diblock polyampholyte (31) and a few model IDP sequences (43), but general design rules are missing to understand the role of charge sequence along a polyampholyte on self-coacervation behavior, independent of variables such as total charge, solvent quality, and molecular weight.

Here, we use field-theoretic simulations to construct complete, approximation-free phase diagrams of block polyampholytes as

Significance

By combining field-theoretic simulations and molecular-dynamics simulations, we show how the charge sequence of block polyampholytes affects their solution-phase behavior and accessible chain conformations. We find a striking effect of like charge block length and connectivity on their self-coacervation or liquid–liquid phase separation. Charge patterning on smaller lengthscales allows for more expanded chain configurations and increased stability in dilute solution. These findings may provide insight into the condensation of intrinsically disordered proteins in vivo.

Author contributions: S.P.O.D., J.M., K.T.D., and G.H.F. designed research; S.P.O.D. and J.M. performed research; S.P.O.D. analyzed data; and S.P.O.D., J.M., J.-E.S., K.T.D., and G.H.F. wrote the paper.

The authors declare no conflict of interest.

This article is a PNAS Direct Submission.

[1]To whom correspondence may be addressed. Email: ghf@ucsb.edu or kdelaney@ucsb.edu.

This article contains supporting information online at www.pnas.org/lookup/suppl/doi:10.1073/pnas.1900435116/-/DCSupplemental.

Published online April 4, 2019.

a function of sequence. The phase diagrams are approximation-free in that they contain no uncontrollable approximations (i.e., analytical or numerical approximations such as closures, mean-field approximations, interaction cutoffs, or simplifications such as neglecting the finite polymer density in the dilute phase), outside of the choice of coarse-grained model. This allows for self-coacervation phenomena to be elucidated as a function of the number of blocks, block asymmetry, and charge asymmetry. In this study, explicit counterions and added salt ions are neglected, but, as we show elsewhere, the inclusion of explicit counterions has only a weak effect on the phase diagrams or structure of charge-neutral polyampholytes in solution, primarily through enhanced electrostatic screening that serves to slightly reduce the effective electrostatic strength. Manipulating the lengthscale and placement of charged patterns are shown to have a strong effect on the structure of the phases, particularly on chain conformations in the dilute branch of phase coexistence. Sequence modulation on the scale of the electrostatic correlation length disrupts self-coacervation, with phase separation maximized for polyampholytes with long runs of like-charged residues and a minimum number of connection points between oppositely charged segments.

Model and Methodology

Molecular Model. In the field theory, we use a coarse-grained model (31, 44–47) of sequence-defined polyampholytes as continuous Gaussian chains, with all pairs of statistical segments interacting through a weak contact excluded volume parameter, v, and charged segments interacting via a Coulomb potential screened by a uniform background dielectric of Bjerrum length, l_B. The interaction energy is

$$\beta\overline{U} = \frac{v}{2}\int d\mathbf{r}\,\overline{\rho}^2(\mathbf{r}) + \frac{l_B}{2}\int d\mathbf{r}\int d\mathbf{r}'\,\frac{\overline{\rho}_e(\mathbf{r})\overline{\rho}_e(\mathbf{r}')}{|\mathbf{r}-\mathbf{r}'|}, \qquad [1]$$

with microscopic density of segment centers, $\hat{\rho}(\mathbf{r}) = \sum_{\alpha=1}^{n}\int ds\,\delta(\mathbf{r}-\mathbf{r}_\alpha(s))$ for n polymer chains and electrostatic charge density, $\hat{\rho}_e(\mathbf{r}) = \sum_{\alpha=1}^{n}\int ds\,\sigma(s)\delta(\mathbf{r}-\mathbf{r}_\alpha(s))$. $\mathbf{r}_\alpha(s)$ is a space curve encoding the configuration of polymer chain α, where s is a continuous backbone contour variable and $\sigma(s)$ is the segmental charge valency density at position s. $\sigma(s)$ is normalized so that its integral along the contour is the total charge per chain in units of the elementary charge, which is zero in all examples shown here.

To ensure that the chemical potentials and pressures calculated in the field-theoretic simulations are insensitive to the computational grid and are free of UV divergences (48, 49), the statistical segments are smeared over a finite volume by convolution with a normalized Gaussian profile, $\Gamma(r) = (2\pi a^2)^{-3/2}\exp(-r^2/2a^2)$ of width a. The smeared microscopic density is then $\overline{\rho}(\mathbf{r}) = \int d\mathbf{r}'\,\Gamma(|\mathbf{r}-\mathbf{r}'|)\hat{\rho}(\mathbf{r}')$, and the smeared electrostatic charge density is $\overline{\rho}_e(\mathbf{r})$.

This interaction energy can be equivalently written in a particle-based representation of bead–spring chains with a nonbonded pair potential between beads separated by a distance r as

$$\beta U(r) = \frac{v}{8\pi^{3/2}a^3}e^{-r^2/4a^2} + \frac{l_B\sigma_i\sigma_j}{r}\mathrm{erf}\Big(\frac{r}{2a}\Big). \qquad [2]$$

The Gaussian smearing in the field theory is seen to translate to a particle model with a soft Gaussian repulsion on the scale of the smearing length a and a Coulomb interaction that is cut off at short distances by an error function with the same range (50, 51). In this implicit solvent model, the v parameter characterizes the solvent quality (larger v implies better solvent quality), while l_B is a measure of the electrostatic strength and is inversely proportional to the solvent dielectric constant. The approach taken to smear both segment and charge densities by a Gaussian function of width a is not an approximation, but simply a model definition. Indeed, this smearing is equivalent to the particle described by Eq. **2**. While well-defined, such a model will not realistically capture liquid structure and electrostatic correlations on angstrom-level monomer and ion-length scales, as segment and ion potentials of mean force are harshly repulsive at close distances. For weakly charged polyelectrolytes with charge spacing greater than the Bjerrum length, this aspect of the model should not influence the results reported here, since structural and electrostatic correlations occur on mesoscopic scales beyond the segment size. In the case of strongly charged polyampholytes, it would seem unlikely that the soft repulsions in the present model would provide a realistic description of phenomena such as counterion condensation and ion pairing. Thus, the reader is cautioned that the trends reported here may not be applicable outside the weakly charged regime.

Field-Theoretic Simulations. Field-theoretic (FTS-CL) and molecular-dynamics (MD) simulations of the corresponding field theory and particle models, respectively, are used to sample the energetic landscape prescribed by the interaction energy of Eqs. **1** and **2** and provide a framework for examining the sequence effects on the structure and thermodynamics of block polyampholytes. The canonical partition function of the model specified in Eq. **1**, integrated over segment coordinates, can be converted via an exact Hubbard–Stratonovich transformation to a complex-valued statistical field theory (44):

$$\mathcal{Z}_c = Z_0\int\mathcal{D}w\int\mathcal{D}\varphi\, e^{-H[w,\varphi]}, \qquad [3]$$

where Z_0 contains the partition function for an ideal gas of continuous Gaussian chains and self-interaction corrections. Model parameters are rescaled by reducing chain-polymerization degrees by a reference N and scaling all spatial lengths by a corresponding ideal homopolymer radius of gyration $R_g = (b^2N/6)^{1/2}$. The field-theoretic Hamiltonian is

$$H[w,\varphi] = \frac{1}{2B}\int d\mathbf{r}\,w^2(\mathbf{r}) + \frac{1}{2E}\int d\mathbf{r}\,|\nabla\varphi(\mathbf{r})|^2 - \frac{CV}{R_g^3}\ln Q[w,\varphi;\overline{a}], \qquad [4]$$

with dimensionless parameters $\overline{a} = a/R_g$, a smearing scale for polymer segments; $B = vN^2R_g^{-3}$, an excluded volume parameter; $C = nR_g^3/V = \rho R_g^3/N$, a polymer chain number density; and $E = 4\pi l_B\sigma^2N^2R_g^{-1}$, a measure of electrostatic interaction strength, with a reference chain charge density σ. For context, a fully charged (i.e., one elementary charge per statistical segment) chain of $N = 100$ in H_2O would have an electrostatic strength $E \sim$ 10,000. This same chain would have a segment concentration of $\rho \sim 2.5$ mol·L^{-1} at $C = 10.0$.

The nonbonded interactions among statistical segments are consequently decoupled, and the segments interact only with auxiliary fields $w(\mathbf{r})$ and $\varphi(\mathbf{r})$, representing the fluctuating excluded volume and electrostatic potentials. The statistics of polymers subject to these fields is described by the single-chain partition function $Q[w,\varphi] = V^{-1}\int d\mathbf{r}\,q(\mathbf{r},1;[w,\varphi])$, where q is a chain propagator that satisfies a modified diffusion equation,

$$\frac{\partial}{\partial s}q(\mathbf{r},s) = [\nabla^2 - \psi(\mathbf{r},s)]\,q(\mathbf{r},s), \qquad [5]$$

with initial condition $q(\mathbf{r},s=0) = 1$. The contour position-dependent field is given by $\psi(\mathbf{r},s) = i\Gamma\star(w + \frac{\sigma(s)}{\sigma}\varphi)$, where $\star$ denotes a spatial convolution.

Electrostatically driven phase separation in charge-neutral polyampholytes cannot be described at the simplest mean-field level; there is no Coulombic contribution to the mean-field free energy of a bulk system with periodic boundary conditions due to global electroneutrality (31, 44–46). Phase separation is only obtained by considering field fluctuations around the electroneutral state (8, 31), through either a Gaussian approximation (RPA) formalism (31, 46, 47) (*SI Appendix*) or field-theoretic simulations that fully sample the field configurations and incorporate all higher-order fluctuation effects (31).

The functional integrals are taken over real-valued $w(\mathbf{r})$ and $\varphi(\mathbf{r})$ fields, but enter the modified diffusion equation for single-chain statistics with imaginary coefficients (44), resulting in an exponentiated H functional that possesses a rapidly oscillating phase. Promoting the fields to be complex variables and using complex Langevin (CL) sampling (52, 53) avoids the efficiency loss associated with this "sign problem." The CL equations of motion used here are

$$\frac{\partial w(\mathbf{r},t)}{\partial t} = -\lambda_w \frac{\delta H[\varphi,w]}{\delta w(\mathbf{r},t)} + \eta_w(\mathbf{r},t), \qquad [6]$$

$$\frac{\partial \varphi(\mathbf{r},t)}{\partial t} = -\lambda_\varphi \frac{\delta H[\varphi,w]}{\delta \varphi(\mathbf{r},t)} + \eta_\varphi(\mathbf{r},t), \qquad [7]$$

where $\eta_i(\mathbf{r},t)$ are real-valued Gaussian-distributed white-noise random variables with statistics $\langle \eta_i(\mathbf{r},t)\rangle = 0$ and $\langle \eta_i(\mathbf{r},t)\eta_i(\mathbf{r}',t')\rangle = 2\lambda_i\delta(\mathbf{r}-\mathbf{r}')\delta(t-t')$. Numerically propagating the CL equations of motion generates importance-sampled sequences of field configurations, and ensemble averages over field-theoretic operators can be replaced by time averages over field samples by the ergodic principle. Numerical details are described in *SI Appendix*.

Phase-equilibrium conditions are constructed through the explicit computation of the osmotic pressure $\Pi(C)$ and chemical potential $\mu(C)$ for a range of concentrations C, and determination of the concentrations at which chemical and mechanical equilibrium conditions can be established between coexisting coacervate and supernatant phases (31). The procedure can be repeated by using RPA estimates (*SI Appendix*) of the chemical potential and pressure in an analogous manner.

MD. The same coarse-grained molecular model used for the field-theoretic simulations can be used to construct MD simulations (43). For the particle simulations, a discrete Gaussian chain model with $N = 100$ is used in contrast to the continuous Gaussian chain model used in the field-theoretic simulations. Single-chain simulations of the polyampholyte in the dilute phase ($C = 0.0001$, the same as used in FTS-CL dilute structure factors) are implemented by using the Large Atomic/Molecular Massively Parallel Simulation software (54), with bonded potential

$$\beta V_{bond}(\tilde{r}) = \frac{1}{4}\tilde{r}^2, \qquad [8]$$

and nonbonded excluded volume and electrostatic interaction potentials

$$\beta U_{ev}(\tilde{r}) = \frac{\tilde{B}}{8\pi^{3/2}\tilde{a}^3} e^{-\tilde{r}^2/4\tilde{a}^2}, \qquad [9]$$

$$\beta U_{el}(\tilde{r}) = \frac{\tilde{E}\sigma_i\sigma_j}{4\pi\tilde{r}} \mathrm{erf}\left(\frac{\tilde{r}}{2\tilde{a}}\right), \qquad [10]$$

where $\tilde{a} = a\sqrt{6}/b$, $\tilde{B} = v\,6^{3/2}/b^3$, and $\tilde{E} = 4\sqrt{6}\pi l_B/b$ are the FTS-CL parameters $\bar{a}$, B, and E, scaled so that the reference $N = 1$ and the fundamental length corresponds to $r_0 = b/\sqrt{6}$. We perform simulations in reduced units $k_B T = 1$ and $\tilde{r} = r/r_0$.

To evaluate the electrostatic potential using mesh-based Ewald summation for Gaussian-smeared charges (55), the real space contribution can be written,

$$\beta U_{el}^{real} = \frac{\sigma_i\sigma_j}{\epsilon\tilde{r}}\left[\mathrm{erf}\left(\frac{\tilde{r}}{2\tilde{a}}\right) - \mathrm{erf}(\aleph\tilde{r})\right], \qquad [11]$$

with $\aleph$ the Ewald screening width in inverse distance units and $\epsilon = 4\pi/E$ the effective dielectric parameter. The error function accounts for the smearing on small lengthscales and serves to regularize the Coulomb interaction at contact. The first term describes interactions among unscreened Gaussian-smeared charges, and the second term subtracts the usual screened point charges that can then be computed in reciprocal space. Written in this way, the reciprocal space expression is the same as that for point charges and is given as

$$\beta\hat{U}^{rec} = \frac{2\pi}{V\epsilon}\sum_{k\neq 0} Q(\mathbf{k})\cdot S(\mathbf{k})S(-\mathbf{k}), \qquad [12]$$

with

$$Q(\mathbf{k}) = \frac{1}{k^2} e^{\frac{-\mathbf{k}^2}{4\aleph^2}}, \qquad [13]$$

$$S(\mathbf{k}) = \sum_{j=1}^{N}\sigma_j e^{i\mathbf{k}\cdot\mathbf{r}_j}, \qquad [14]$$

which is the usual Ewald summation (56, 57).

As explored in detail elsewhere, particle MD simulation provides an opportunity to supplement the FTS-CL simulations with structural information regarding single-chain conformations (43).

Chain Conformation Analysis. The conformations of the polymer chains are analyzed by using shape parameters that are defined by means of the invariants of the gyration tensor $\boldsymbol{S}$.

$$S_{ij} = \frac{1}{N}\sum_{k=1}^{N}(r_{k,i} - r_{\mathrm{com},i})(r_{k,j} - r_{\mathrm{com},j}), \qquad [15]$$

where $r_{\mathrm{com},i}$ is the ith Cartesian component of the chain center of mass and $r_{k,i}$ is the ith component of the position of segment k. Transformation to the principal axis system diagonalizes $\boldsymbol{S}$,

$$\boldsymbol{S} = \mathrm{diag}(\lambda_1,\lambda_2,\lambda_3), \qquad [16]$$

where we assume that the eigenvalues of $\boldsymbol{S}$ are sorted in descending order, i.e., $\lambda_1 \geq \lambda_2 \geq \lambda_3$. The first invariant of $\boldsymbol{S}$ gives the squared radius of gyration,

$$R_g^2 = \lambda_1 + \lambda_2 + \lambda_3 = \mathrm{Tr}\,\boldsymbol{S}. \qquad [17]$$

The second invariant shape descriptor, or relative shape anisotropy, is defined as

$$\begin{aligned}\kappa^2 &\equiv \frac{3}{2}\frac{\mathrm{Tr}\,\hat{\boldsymbol{S}}^2}{(\mathrm{Tr}\,\boldsymbol{S})^2} = 1 - 3\frac{I_2}{I_1} \\ &= 1 - 3\frac{\lambda_1\lambda_2 + \lambda_2\lambda_3 + \lambda_3\lambda_1}{(\lambda_1+\lambda_2+\lambda_3)^2} \\ &= \frac{3}{2}\frac{\lambda_1^2+\lambda_2^2+\lambda_3^2}{(\lambda_1+\lambda_2+\lambda_3)^2} - \frac{1}{2},\end{aligned} \qquad [18]$$

where $\hat{\boldsymbol{S}} = \boldsymbol{S} - 1/3(\mathrm{Tr}\,\boldsymbol{S})\boldsymbol{E}$ with unit tensor $\boldsymbol{E}$. The anisotropy κ^2 reflects both the symmetry and dimensionality of a polymer conformation. This parameter is restricted to values between 0 and 1. It reaches 1 for an extended linear configuration and 0 for highly spherically symmetric conformations.

Single-Chain Structure Factor. The single-chain structure factor (58) of an isolated polyampholyte chain in the dilute supernatant is given by

$$P(\mathbf{k}) = \frac{1}{N}\left\langle \left[\sum_{i=1}^{N}\cos\left(\mathbf{k}\cdot\mathbf{r}_i\right)\right]^2 + \left[\sum_{i=1}^{N}\sin\left(\mathbf{k}\cdot\mathbf{r}_i\right)\right]^2 \right\rangle, \quad [19]$$

where the periodic boundary conditions render the quantized wave vectors $\mathbf{k} = 2\pi(n_x, n_y, n_z)/L$ with n_x, n_y, and n_z integers.

Results and Discussion

Work on the sequence effects or molecular design of complex coacervates or self-coacervates have focused thus far on differences in charge pattern that mimic those found in IDPs (43), relying on characterizing a sequence by a charge pattern metric such as

$$SCD = \frac{1}{N}\left[\sum_{m=2}^{N}\sum_{n=1}^{m-1}\sigma_m\sigma_n(m-n)^{1/2}\right], \quad [20]$$

of Sawle and Ghosh (59) or κ of Das and Pappu (60). However, this convolutes several distinct molecular parameters into a single metric. Here, we develop more comprehensive design principles for the effects of block number (or, inversely, block length at fixed polymer degree of polymerization), the symmetry or patterning of those blocks, and, finally, asymmetry in how the charge is distributed among the blocks. We present phase diagrams independently controlling each of these molecular features. Our phase diagrams are dependent on three dimensionless parameters, a polymer chain density C, an excluded-volume parameter B, and an electrostatic strength E. Importantly for H_2O, it is natural to present them as E vs. C, in an analogous way to experimental phase diagrams (e.g., ionic strength vs. polymer concentration). Here, we will present phase diagrams at low electrostatic strengths to highlight near-critical-point behavior. We begin by sweeping B for a simple diblock polyampholyte to see the sensitivity of the two-phase region to the overall solvent quality before focusing on sequence and architecture effects.

Excluded Volume. Solvent quality is often a function of concentration, temperature, and even sequence due to the arrangement of hydrophilic and hydrophobic residues. Even specific ion effects can impact solvent quality, depending on the particular ion identity. Since the solvent quality may change as a function of such variables, we first present the effect of solvent quality/excluded volume on the phase diagram of the diblock polyampholyte $\mathcal{A}_{50}\mathcal{C}_{50}$ and show that binodals are shifted in a predictable manner (Fig. 1). To simplify descriptions of the charge-sequence patterns, we use a nomenclature where $\mathcal{A}$ represents the negatively charged block and $\mathcal{C}$ the positively charged block, and the subscripts are the length of the like-charged block out of 100 contour steps ($\Delta s = 0.01$; *SI Appendix*). $\mathcal{A}_{50}\mathcal{C}_{50}$ is thus a charge-neutral diblock polyampholyte of uniform and opposite valence on the two blocks. Recall that the overall charge density σ enters in the electrostatic strength E.

Increasing the excluded volume parameter $B = 0.5, 1.0, 2.0, 5.0$ reflects increasing solvent quality. Better solvent-quality conditions suppress the thermodynamic instability that causes self-coacervation since excluded volume interactions are repulsive, swelling the chains and resisting the attractive electrostatic forces responsible for condensation and phase separation into a dense coacervate. Thus, over a range of good solvents ($v > 0$), the critical electrostatic strength (E_c) increases in a predictable and modest manner with increasing excluded volume, in agreement with other theoretical approaches (61–63).

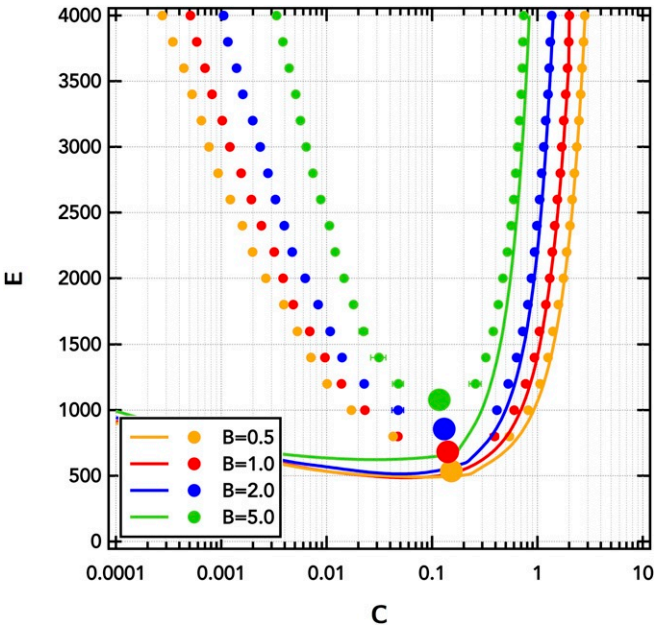

Fig. 1. Effect of excluded volume parameter, *B*, on the phase diagram of diblock polyampholyte, $\mathcal{A}_{50}\mathcal{C}_{50}$, showing predictable shrinking of the two-phase region with increasing solvent quality. Symbols are binodal points obtained from FTS-CL, and lines are RPA predictions. The Gaussian smearing width is set at $\bar{a} = 0.2$.

In addition to shifting toward higher electrostatic strengths, the two-phase region of the phase window narrows with increasing B. This narrowing occurs on both the concentrated and dilute branches. Recall that the coexistence conditions are dictated by chemical, $\mu^I = \mu^{II}$, and mechanical, $\Pi^I = \Pi^{II}$, equilibrium. Higher B leads to higher $d\mu/dC$ and $d\Pi/dC$ penalties due to excluded volume, particularly in the concentrated phase. The dilute branch of the binodal curve shifts inward (toward higher polymer concentration) to compensate. However, this narrowing remains stronger on the concentrated branch, as evidenced by the extrapolated critical polymer concentration (i.e., C at the critical point; see *SI Appendix* for extrapolation procedure) shifting to lower values.

RPA predictions shown in Fig. 1 qualitatively capture the narrowing of the two-phase window with increasing excluded volume, including quantitatively capturing the behavior at high C. However, due to the catastrophic failure on the dilute branch, the RPA underestimates the effects on the critical point, a failure that worsens with increasing B.

Even at a relatively weak electrostatic strength, $E = 1{,}000$ (recall N^2 dependence), the chain conformations in the dilute solution (left of the two-phase region in Fig. 1; $C = 0.0001$) are dominated by electrostatics with compact radii of gyration, R_g, and globular-like configurations (*SI Appendix*, Fig. S5). Thus, the excluded volume effects on the isolated chains are comparatively weak, and the polyampholytes corresponding to different B values have nearly identical structure (*SI Appendix*, Figs. S2–S4). This confirms that the effects of excluded volume on isolated polyampholytes in the dilute phase are relatively unimportant; even though the local densities are comparable, the dilute-phase effects on the binodal are due to propagation of chemical and mechanical equilibrium conditions due to osmotic pressure and chemical potential increases in the concentrated phase.

As argued above, the phase behavior is dominated by the concentrated phase, where overlapping polyampholytes with increasing excluded volume is strongly penalized, resulting in

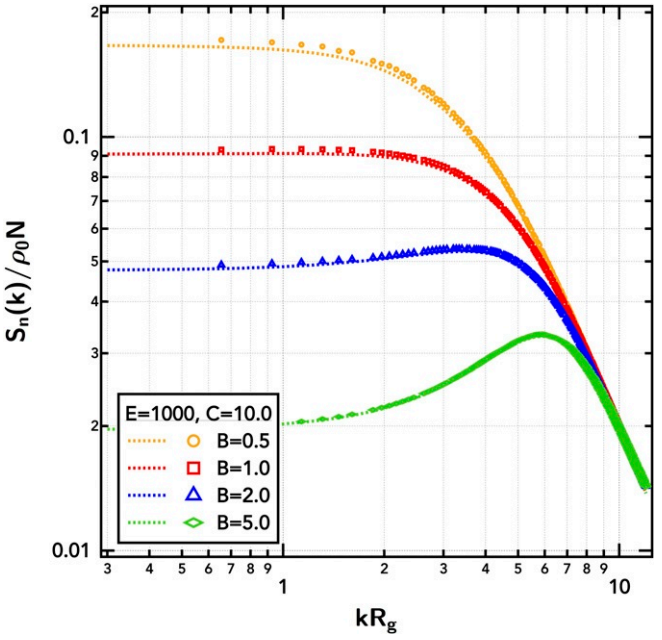

Fig. 2. Total density structure factor, $S_n(k)$, in the concentrated phase as a function of the excluded volume parameter, showing decreased isothermal compressibility with increasing B. Symbols are obtained from FTS-CL, and lines are RPA predictions. The Gaussian smearing width is set at $\bar{a} = 0.2$.

coacervates of lower concentration. An increase in B leads to a sharp decrease in the isothermal compressibility ($S_n^{RPA}(0) \propto \frac{1}{1+BC}$) and the emergence of a well-defined correlation length (Fig. 2). By asymptotic expansion of the RPA result for the total density structure factor $S_n(k)$ at high k, this correlation length is $\xi_E = (2BC)^{-1/2}$, the Edwards correlation length as in neutral polymer solutions. This is the lengthscale over which segment density fluctuations are correlated; i.e., blobs of size ξ_E fluctuate independently.

The structure factors indicate that charge and mass fluctuations are practically decoupled (and are strictly so in RPA), such that ξ_E is not impacted by the charge pattern because the positive and negative segments have equivalent excluded volume interactions in this model; there is no excess chemical incompatibility or χ parameter between the segments of cationic and anionic charge. This framework can be readily extended to these scenarios, but is outside the scope of this work on sequence effects. For the remainder of this work, we will fix $B = 1$.

Block Length and Number. The clustering of like charges into local patches amplifies electrostatic fluctuations, while the scrambling of those charges diminishes phase separation (13, 32). We probe this sequence effect on the self-coacervation behavior by tuning the "blockiness" or block length and number in an alternating positively and negatively charged block polyampholyte, where the blocks are of uniform, equal, and opposite valences. We increase the block number N_B over the sequence $2, 4, 6, 10$ ($SCD = -78.3, -24.4, -16.2, -5.4$). Here, as in the entire work, we constrain constant chain length and zero net total charge; thus, with increasing block number, the length of each block decreases $\frac{l_{block}}{N} = \frac{1}{2}, \frac{1}{4}, \frac{1}{6}, \frac{1}{10}$ and the number of connection points N_{A-C} increases as $1, 3, 5, 9$. Furthermore, increasing the blockiness over a wide range allows us to probe the transition from a block polyampholyte to the alternating polyampholyte limit.

The number and length of the block charge pattern has a substantial effect on the phase diagram, with shorter blocks significantly suppressing phase separation (Fig. 3). There is a dramatic increase in the critical electrostatic strength, which increases by an order of magnitude from the diblock polyampholyte ($\mathcal{A}_{50}\mathcal{C}_{50}$) to the decablock polyampholyte ($\mathcal{A}_{10}\mathcal{C}_{10}\mathcal{A}_{10}\mathcal{C}_{10}\mathcal{A}_{10}\mathcal{C}_{10}\mathcal{A}_{10}\mathcal{C}_{10}\mathcal{A}_{10}\mathcal{C}_{10}$).

While there is a minor effect on the concentrated branch that is primarily due to the difference in critical electrostatic strength, the concentrated phase is relatively agnostic to the charge pattern. This is because in the coacervate phase, the characteristic lengthscales of density, ξ_E, and electrostatic, ξ_e, fluctuations are smaller than the lengthscale of the patterning (i.e., smaller than the block length until approaching the alternating or random copolymer limit). This is evidenced by the comparable density–density structure factors (*SI Appendix*, Fig. S6) and nearly the same peak wavevector in the electrostatic structure factor (*SI Appendix*, Fig. S7) for all block lengths at $C = 10.0$. Interestingly, the intensity of the electrostatic correlations does decrease slightly with increasing block number. We attribute this to packing entropy differences of the oppositely charged blobs in concentrated solution due to their different chain connectivity.

The largest effect, however, is on the dilute branch, where the binodal curve sweeps inward to higher polymer concentration over three orders of magnitude, significantly narrowing the two-phase region as the number of blocks is increased and the length of the charge repeat is decreased. Recall the RPA prediction of the electrostatic correlation length in units of R_g, $\xi_e \sim (2EC)^{-1/4}$ (45). In the concentrated phase, ξ_e is much smaller than the block radius of gyration, reflecting electrostatic screening of highly overlapping coils. In contrast, in dilute solution, the correlation length is increased and can be similar or larger in scale relative to the size of the blocks. Nonetheless, as the block size is decreased, the length of the block impinges on ξ_e at dilute conditions (Fig. 4*B*). This impingement creates additional electrostatic screening that stabilizes increased concentration of the polyampholytes in the dilute branch (supernatant), shifting

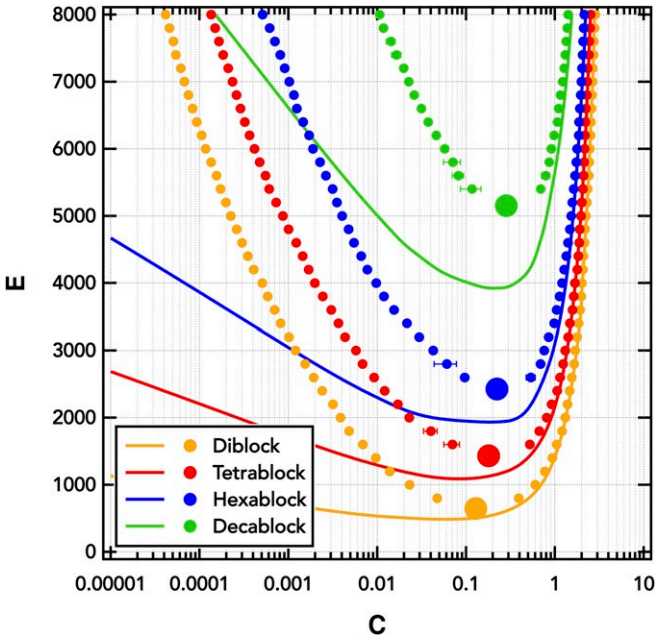

Fig. 3. Phase diagram showing the dramatic effect of decreasing block length in narrowing the two-phase region and increasing the critical electrostatic strength. Symbols are binodal points obtained from FTS-CL, and lines are RPA predictions. The Gaussian smearing width is set at $\bar{a} = 0.2$ and the excluded volume parameter at $B = 1$.

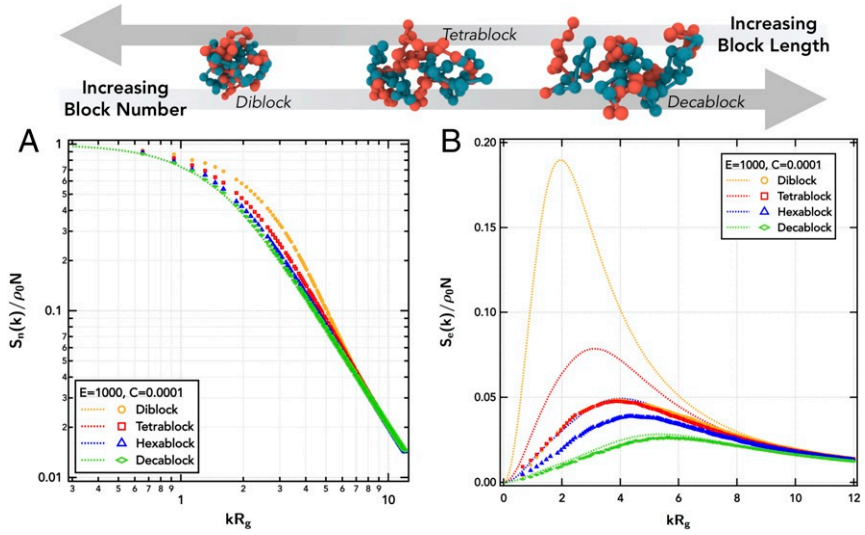

Fig. 4. Total density structure factor, $S_n(k)$ (*A*), and charge-weighted structure factor, $S_e(k)$ (*B*), in the dilute supernatant as a function of the number of blocks, N_B. Symbols are obtained from FTS-CL, and lines are RPA predictions. ξ_e decreases with decreasing block size. The Gaussian smearing width is set at $\bar{a} = 0.2$ and the excluded volume parameter at $B = 1$. The visualized polyampholyte chains (orange beads, negatively charged; teal beads, positively charged) are representative snapshots from MD simulations.

the binodal curve to higher E and C. The catastrophic failure of RPA in predicting the dilute binodal branches is seen again in Fig. 3 and in the dilute electrostatic structure factors of Fig. 4*B*.

The thermodynamic properties of the polyampholytes in the dilute phase are further influenced by the chain conformations accessible by each sequence. The diblock polyampholyte has little choice but to collapse to a charge-neutral globule. However, as the number of blocks is increased, the charge neutrality can be satisfied on a more local scale, allowing for swelling and greater conformational freedom. The density–density structure factor from FTS-CL (Fig. 4*A*), as well as the configuration snapshots (Fig. 4), single-chain structure factor (*SI Appendix*, Fig. S8), and gyration tensor metrics (*SI Appendix*, Fig. S9) from MD, all capture this increase in the number of conformational states accessible and show an increase in R_g due to the conformational relaxation. This increased entropy stabilizes the dilute polyampholyte solution, resisting electrostatic correlations that drive condensation into a coacervate.

Block Asymmetry. To understand the importance of block number on the phase behavior and structure of block polyampholytes, we split the chain into an increasing number of smaller blocks. However, it is important to distinguish the effects of block size and symmetry from the number of A–C connecting junctions. This can be achieved by interrogating a triblock polyampholyte of form ACA′ and varying the relative length of the A and A′ blocks. This block asymmetry can be described by an asymmetry factor,

$$\tau \equiv \frac{|f - f'|}{f + f'}, \qquad [21]$$

where f and f' are the lengths of the A and A′ blocks. For a charge-neutral block polyampholyte, the block-asymmetry factor varies from $\tau = 0$ for a symmetric ACA triblock polyampholyte to $\tau = 1$, the highly asymmetric limit of the diblock polyampholyte. Here, we highlight the effects of block asymmetry on self-coacervation by comparing the phase diagrams of $\mathcal{A}_{25}\mathcal{C}_{50}\mathcal{A}_{25}$ ($\tau = 0$, $SCD = -31.3$), $\mathcal{A}_{35}\mathcal{C}_{50}\mathcal{A}_{15}$ ($\tau = 0.4$, $SCD = -38.6$), and $\mathcal{A}_{45}\mathcal{C}_{50}\mathcal{A}_{5}$ ($\tau = 0.8$, $SCD = -61.0$) against $\mathcal{A}_{50}\mathcal{C}_{50}$ ($\tau = 1$, $SCD = -78.3$) (Fig. 5).

The block-asymmetry effect is far more subtle than the changes to phase behavior from changing the number of blocks and is not properly captured by the SCD metric. The concentration of the coacervate phase is effectively identical across a range of τ, as would be expected by the similar structure of these polyampholytes in the highly overlapping chain configurations within the concentrated self-coacervate (identical $S_n(k)$; *SI Appendix*, Fig. S10). Again, we see that the local charge patterning produces the same lengthscale for electrostatic fluctuations, ξ_e, but with a different intensity of those correlations due to packing entropy from the different number of connecting points

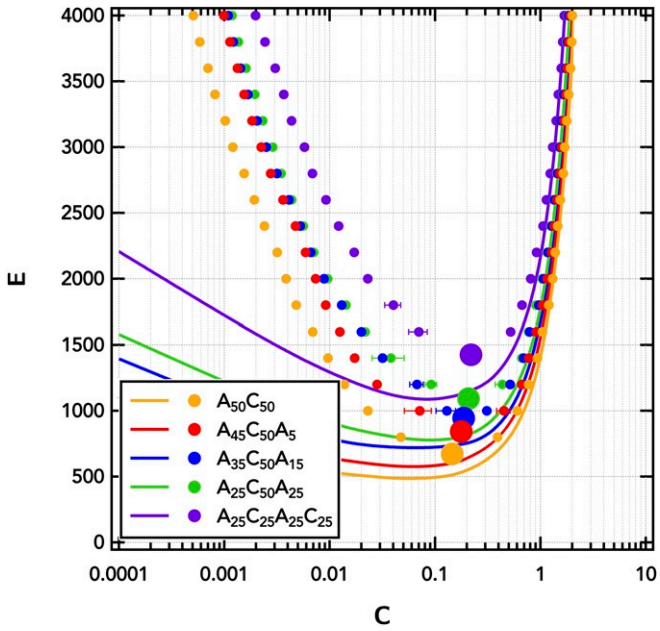

Fig. 5. Phase diagram showing the importance of the number of connecting points at high E and block symmetry near the critical point. Symbols are binodal points obtained from FTS-CL, and lines are RPA predictions. The Gaussian smearing width is set at $\bar{a} = 0.2$ and the excluded volume parameter at $B = 1$.

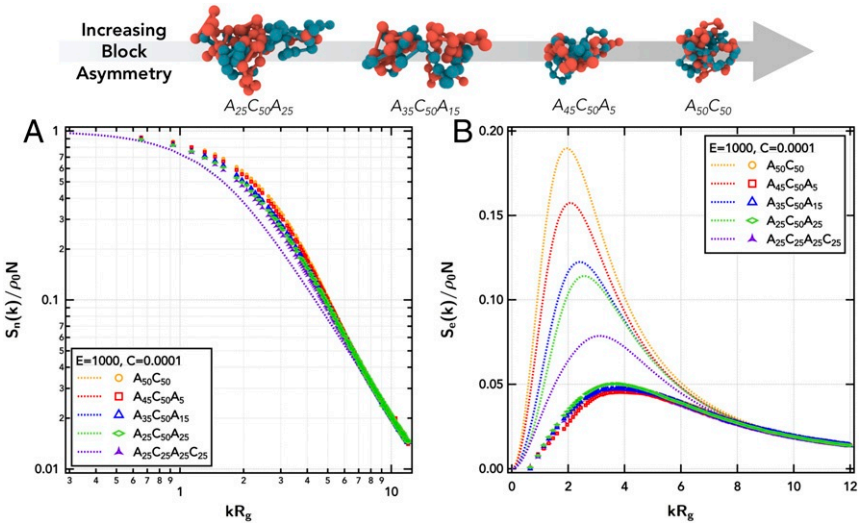

Fig. 6. Total density structure factor, $S_n(k)$ (*A*), and charge-weighted structure factor, $S_e(k)$ (*B*), in the dilute supernatant as a function of block symmetry. Symbols are obtained from FTS-CL, and lines are RPA predictions. The Gaussian smearing width is set at $\bar{a} = 0.2$ and the excluded volume parameter at $B = 1$. The visualized polyampholyte chains (orange beads, negatively charged; teal beads, positively charged) are representative snapshots from MD simulations.

for the triblock polyampholytes vs. the diblock polyampholyte (*SI Appendix*, Fig. S11).

Interestingly, the dilute branch saturates to the same binodal concentrations at high E for all of the triblock polyampholytes, but distinct from the diblock and tetrablock polyampholytes. Thus, the dilute behavior at high electrostatic strengths is dictated by the number of connecting points between oppositely charged residues. This is a remarkable result, as even small patches of oppositely charged segments can induce a significant difference in phase behavior at strong electrostatic strengths. The additional connection point must affect the local packing of a single coil, which, in the strong electrostatic limit, results in a reduced set of accessible chain conformations. As the electrostatic strength is lowered (decreasing E) toward the critical point, the block asymmetry has an even greater influence on the phase behavior. Near the critical point, the behavior transitions continuously from a symmetric triblock ($\mathcal{A}_{25}\mathcal{C}_{50}\mathcal{A}_{25}$) down to a diblock polyampholyte ($\mathcal{A}_{50}\mathcal{C}_{50}$). The critical electrostatic strength decreases with block asymmetry, as does the critical polymer concentration. Examining the chain conformations of the polyampholytes in the supernatant confirms this interpretation. The more asymmetric block polyampholytes have smaller R_g (Fig. 6*A* and *SI Appendix*, Figs. S12 and S13) and more isotropic configurations (*SI Appendix*, Fig. S13), as the larger coherent blocks penalize extended conformations.

The dilute solutions of the block-asymmetric polyampholytes further have similar ξ_e (Fig. 6*B*), which decreases slightly with block asymmetry. Interestingly, this is the opposite trend of that predicted by RPA, possibly a consequence of miscapturing intramolecular correlations, as has been recently suggested (36, 64). However, one should expect ξ_e to decrease with increasing block asymmetry, as the length of the A' block impinges upon the unperturbed lengthscale for electrostatic fluctuations, as seen with the effect of block length. This is supported by the nearly equivalent $S_e(k)$ of $\mathcal{A}_{50}\mathcal{C}_{50}$ and $\mathcal{A}_{45}\mathcal{C}_{50}\mathcal{A}_5$. The RPA is again seen to grossly overpredict the amplitude of $S_e(k)$ across this dilute series.

Charge Asymmetry. There is another symmetry that can be affected by the patterning of the individual sequence: charge density along the chain. Here, we maintain overall charge neutrality, but increase the charge density of one block with a compensating reduction in block length. We compare a charge-asymmetric polyampholyte $\mathcal{A}_{75}^{-2/3}\mathcal{C}_{25}^{+2}$ ($SCD = -80.5$) to the charge-symmetric $\mathcal{A}_{50}^{-1}\mathcal{C}_{50}^{+1}$ ($SCD = -78.3$). The superscripts in this notation represent the block-charge valency.

We find only a very weak effect on the phase diagram by altering the charge-density symmetry, reinforcing the importance of connectivity and balanced total charge and suggesting the relative unimportance in how finely the charge is packed within blocks, at a fixed total polymeric charge (Fig. 7). The result is a near-identical critical electrostatic strength. The two-phase region is shifted by charge-density asymmetry to slightly lower

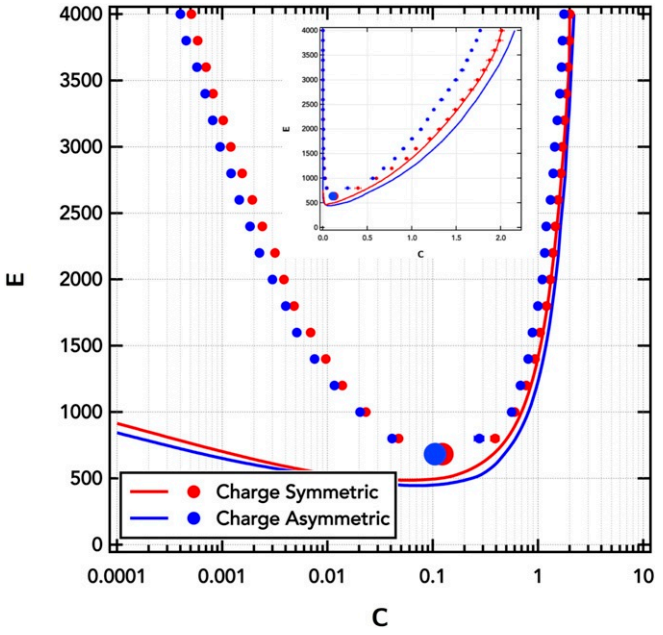

Fig. 7. Phase diagram showing the weak effects of charge-density symmetry. Symbols are binodal points obtained from FTS-CL, and lines are RPA predictions. The Gaussian smearing width is set at $\bar{a} = 0.2$ and the excluded volume parameter at $B = 1$. (*Inset*) Linearly scaled concentration axis to highlight the failure of RPA in predicting the concentrated phase binodal conditions for the charge-asymmetric polyampholyte, $\mathcal{A}_{75}^{-2/3}\mathcal{C}_{25}^{+2}$.

polymer concentration throughout the phase diagram, suggesting stronger correlations that induce electrostatic attractions at lower polymer concentration in the dilute phase, but more electrostatic screening in the concentrated phase.

As expected, there is catastrophic failure of the RPA on the dilute branch, but, interestingly, the RPA also fails to capture behavior of the charge-asymmetric block polyampholyte at high C, where it is expected to be valid. The origin of this failure is unknown: The RPA is accurate in predicting the osmotic pressure (*SI Appendix*, Fig. S14) and structure of the coacervate phase (Fig. 8*B* and *SI Appendix*, Fig. S16), but fails to predict the chemical potential of the charge-asymmetric polyampholyte, showing deviations between RPA and FTS-CL, even at high C (*SI Appendix*, Fig. S15), possibly due to more intense local ion-pair correlations.

In the coacervate, the charge-symmetric and -asymmetric polyampholytes maintain the same total density correlations, but the charge-asymmetric case has stronger intensity of electrostatic correlations, likely due to the increased localized charge density, with a slightly smaller ξ_e due to enhanced screening from the higher localized charge.

As with previous alterations of the molecular structure, the differences in the thermodynamics correlate with conformational changes in the dilute supernatant. FTS-CL shows that the dilute-phase total-density structure factor, $S_n(k)$, is nearly the same for the charge-symmetric and -asymmetric cases (*SI Appendix*, Fig. S17), but the single-chain MD simulations show the existence of significantly more compact globules (Fig. 8 and *SI Appendix*, Figs. S18 and S19). Evidently, in the asymmetric case, the more intense electrostatic correlations between blocks have overcome the Gaussian excluded volume repulsions to a larger extent than in the charge-symmetric polyampholyte. This conclusion is supported by the longer lengthscale and more intense electrostatic correlations of the charge-asymmetric polyampholyte in the dilute solution. However, RPA fails to predict the dominant lengthscale of those correlations. FTS-CL shows a longer lengthscale ξ_e in the charge-asymmetric case, while RPA predicts a smaller ξ_e.

Conclusions

Approximation-free phase diagrams have been developed for the effects of excluded volume, block length and number, block symmetry, and charge symmetry on the self-coacervation behavior of block polyampholytes. This phase behavior and structural insights into both dilute and concentrated phases are made possible by a unique combination of field-theoretic and MD simulations of the same underlying molecular model. [Note: The FTS-CL simulations and RPA predictions use continuous Gaussian chains, while the MD particle simulations use discrete Gaussian chains; the discretization of the chain is expected to be unimportant (43, 45, 46)].

Block length in particular has a large effect on the critical electrostatic strength for phase separation due to impingement on the electrostatic correlation length and increased charge screening as the block length decreases. Manipulating the asymmetry of the block placement or size highlights the importance of the number of chain-connection points and ability to control phase separation by the patterning lengthscale.

As seen in complex coacervation of oppositely charged polyelectrolytes (65), we have found a strong effect of charge pattern on the thermodynamics and materials structure. However, simplified charge sequence metrics like SCD (59), while successful in capturing trends of the critical electrostatic strength and R_g (43), are found to be insufficient in predicting the full phase coexistence behavior of sequence-defined polyampholytes. These studies on molecular-design principles utilizing an implicit solvent, charge-neutral polyampholyte model without counterions reveal a complex interplay of charge sequence with chain conformations and electrostatic correlations in both dilute and concentrated phases. FTS-CL simulations of charge-neutral polyampholytes with explicit counterions reveal very small variations from the counterion-free results presented here. As a result, we do not attribute sequence-dependent trends to differences in entropic confinement of condensed counterions as suggested by Sing, Perry, and coworkers (65), although such effects could potentially be present at high charge density in systems containing counterions.

The sequence-specific effects have the largest influence on the dilute phase. The charge distribution alters charge–charge correlations and dramatically influences coil dimensions and their propensity for self-aggregation, thus impacting the dilute branch of the coexistence region and the overall stability of polyampholyte in the solution.

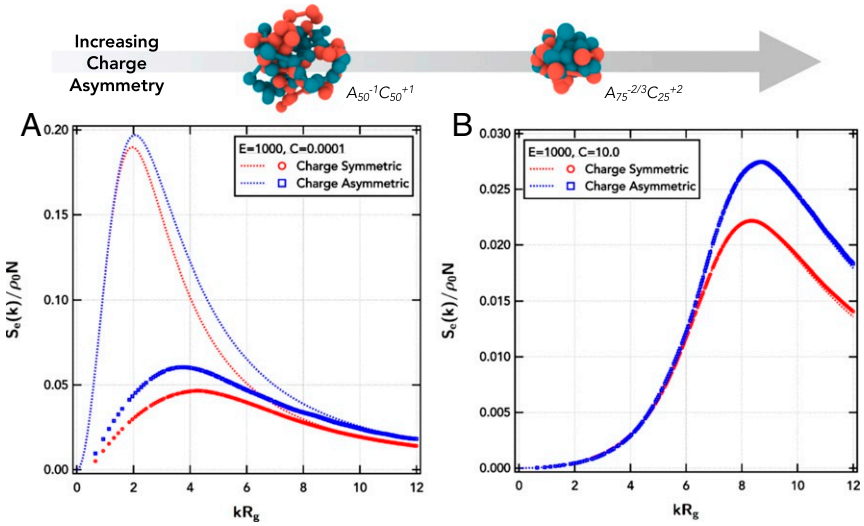

Fig. 8. Charge-weighted structure factor, $S_e(k)$, in the dilute (*A*) and concentrated (*B*) phases as a function of charge symmetry. Symbols are obtained from FTS-CL, and lines are RPA predictions. The Gaussian smearing width is set at $\bar{a} = 0.2$ and the excluded volume parameter at $B = 1$. The visualized polyampholyte chains (orange beads, negatively charged; teal beads, positively charged) are representative snapshots from MD simulations.

ACKNOWLEDGMENTS. This work was supported by the Materials Research Science and Engineering Centers (MRSEC) Program of the National Science Foundation (NSF) through Award DMR-1720256 (IRG-3). J.-E.S. received partial support from NSF Award MCB-1716956. J.M. and J.-E.S. were partially supported by the National Institutes of Health Grant R01AG05605. All simulations were performed by using computational facilities of the Extreme Science and Engineering Discovery Environment (XSEDE; supported by NSF Project TG-MCA05S027) and of the Center for Scientific Computing from the California NanoSystems Institute, Materials Research Laboratory: NSF MRSEC Grant DMR-1720256 and NSF Grant CNS-1725797.

1. Dobrynin AV, Colby RH, Rubinstein M (2004) Polyampholytes. *J Polym Sci B Polym Phys* 42:3513–3538.
2. Everaers R, Johner A, Joanny JF (1997) Polyampholytes: From single chains to solutions. *Macromolecules* 30:8478–8498.
3. Patrickios CS, Strittmatter JA, Hertler WR, Hatton TA (1996) Aqueous size exclusion chromatography of random, diblock, and ABC triblock methacrylic polyampholytes. *J Colloid Interf Sci* 182:326–329.
4. Ohlemacher A, Candau F, Munch JP, Candau SJ (1996) Aqueous solution properties of polyampholytes: Effect of the net charge distribution. *J Polym Sci B Polym Phys* 34:2747–2757.
5. Samanta HS, Chakraborty D, Thirumalai D (2018) Charge fluctuation effects on the shape of flexible polyampholytes with applications to intrinsically disordered proteins. *J Chem Phys* 149:163323.
6. Gonzalezmozuelos P, Delacruz MO (1994) Random-phase-approximation for complex charged systems—application to copolyelectrolytes (polyampholytes). *J Chem Phys* 100:507–517.
7. Jiang J, Feng J, Liu H, Hu Y (2006) Phase behavior of polyampholytes from charged hard-sphere chain model. *J Chem Phys* 124:144908.
8. Castelnovo M, Joanny JF (2002) Phase diagram of diblock polyampholyte solutions. *Macromolecules* 35:4531–4538.
9. Shusharina NP, Zhulina EB, Dobrynin AV, Rubinstein M (2005) Scaling theory of diblock polyampholyte solutions. *Macromolecules* 38:8870–8881.
10. Wang ZW, Rubinstein M (2006) Regimes of conformational transitions of a diblock polyampholyte. *Macromolecules* 39:5897–5912.
11. Lin YH, Brady JP, Forman-Kay JD, Chan HS (November 10, 2017) Charge pattern matching as a 'fuzzy' mode of molecular recognition for the functional phase separations of intrinsically disordered proteins. *New J Phys*, 10.1088/1367-2630/aa9369.
12. Lin YH, Song JH, Forman-Kay JD, Chan HS (2017) Random-phase-approximation theory for sequence-dependent, biologically functional liquid-liquid phase separation of intrinsically disordered proteins. *J Mol Liq* 228:176–193.
13. Lin YH, Forman-Kay JD, Chan HS (2016) Sequence-specific polyampholyte phase separation in membraneless organelles. *Phys Rev Lett* 117:178101.
14. Das S, Eisen A, Lin YH, Chan HS (2018) A lattice model of charge-pattern-dependent polyampholyte phase separation. *J Phys Chem B* 122:5418–5431.
15. Uversky VN, Gillespie JR, Fink AL (2000) Why are natively unfolded proteins unstructured under physiologic conditions? *Proteins Struct Funct Genet* 41: 415–427.
16. Tompa P (2012) Intrinsically disordered proteins: A 10-year recap. *Trends Biochem Sci* 37:509–516.
17. Forman-Kay JD, Mittag T (2013) From sequence and forces to structure, function, and evolution of intrinsically disordered proteins. *Structure* 21:1492–1499.
18. van der Lee R, et al. (2014) Classification of intrinsically disordered regions and proteins. *Chem Rev* 114:6589–6631.
19. Higgs PG, Joanny JF (1991) Theory of polyampholyte solutions. *J Chem Phys* 94:1543–1554.
20. Brangwynne CP, et al. (2009) Germline P granules are liquid droplets that localize by controlled dissolution/condensation. *Science* 324:1729–1732.
21. Li P, et al. (2012) Phase transitions in the assembly of multivalent signalling proteins. *Nature* 483:336–340.
22. Kato M, et al. (2012) Cell-free formation of RNA granules: Low complexity sequence domains form dynamic fibers within hydrogels. *Cell* 149:753–767.
23. Lee CF, Brangwynne CP, Gharakhani J, Hyman AA, Julicher F (2013) Spatial organization of the cell cytoplasm by position-dependent phase separation. *Phys Rev Lett* 111:088101.
24. Nott TJ, et al. (2015) Phase transition of a disordered nuage protein generates environmentally responsive membraneless organelles. *Mol Cell* 57:936–947.
25. Dundr M, Misteli T (2010) Biogenesis of nuclear bodies. *Cold Spring Harbor Perspect Biol* 2:a000711.
26. Toretsky JA, Wright PE (2014) Assemblages: Functional units formed by cellular phase separation. *J Cell Biol* 206:579–588.
27. Hyman AA, Weber CA, Juelicher F (2014) Liquid-liquid phase separation in biology. *Annu Rev Cell Dev Biol* 30:39–58.
28. Elbaum-Garfinkle S, et al. (2015) The disordered P granule protein LAF-1 drives phase separation into droplets with tunable viscosity and dynamics. *Proc Natl Acad Sci USA* 112:7189–7194.
29. Brangwynne CP, Tompa P, Pappu RV (2015) Polymer physics of intracellular phase transitions. *Nat Phys* 11:899–904.
30. Wright PE, Dyson HJ (2015) Intrinsically disordered proteins in cellular signalling and regulation. *Nat Rev Mol Cell Biol* 16:18–29.
31. Delaney KT, Fredrickson GH (2017) Theory of polyelectrolyte complexation-complex coacervates are self-coacervates. *J Chem Phys* 146:224902.
32. Pak CW, et al. (2016) Sequence determinants of intracellular phase separation by complex coacervation of a disordered protein. *Mol Cell* 63:72–85.
33. Cheong DW, Panagiotopoulos AZ (2005) Phase behaviour of polyampholyte chains from grand canonical Monte Carlo simulations. *Mol Phys* 103:3031–3044.
34. Overbeek JT, Voorn MJ (1957) Phase separation in polyelectrolyte solutions. Theory of complex coacervation. *J Cell Comp Physiol Suppl* 49:7–22; discussion, 22–26.
35. Qin J, de Pablo JJ (2016) Criticality and connectivity in macromolecular charge complexation. *Macromolecules* 49:8789–8800.
36. Friedowitz S, Salehi A, Larson RG, Qin J (2018) Role of electrostatic correlations in polyelectrolyte charge association. *J Chem Phys* 149:163335.
37. Everaers R, Johner A, Joanny JF (1997) Complexation and precipitation in polyampholyte solutions. *Europhys Lett* 37:275–280.
38. Barbosa MC, Levin Y (1996) Phase transitions of a neutral polyampholyte. *Phys A* 231:467–483.
39. Corpart JM, Candau F (1993) Aqueous-solution properties of ampholytic copolymers prepared in microemulsions. *Macromolecules* 26:1333–1343.
40. Goloub T, de Keizer A, Stuart MAC (1999) Association behavior of ampholytic diblock copolymers. *Macromolecules* 32:8441–8446.
41. Patrickios CS, Hertler WR, Abbott NL, Hatton TA (1994) Diblock, ABC triblock, and random methacrylic polyampholytes: Synthesis by group-transfer polymerization and solution behavior. *Macromolecules* 27:930–937.
42. Mccormick CL, Johnson CB (1990) Water-soluble polymers: 33. Ampholytic terpolymers of sodium 2-acrylamido-2-methylpropanesulfonate with 2-acrylamido-2-methylpropanedimethylammonium chloride and acrylamide: Synthesis and aqueous-solution behavior. *Polymer* 31:1100–1107.
43. McCarty J, Delaney KT, Danielsen SPO, Fredrickson GH, Shea J-E (March 15, 2019) Complete phase diagram for liquid-liquid phase separation of intrinsically disordered proteins. *J Phys Chem Lett*, 10.1021/acs.jpclett.9b00099.
44. Fredrickson GH (2006) *The Equilibrium Theory of Inhomogeneous Polymers* (Oxford Univ Press, Oxford).
45. Popov YO, Lee JH, Fredrickson GH (2007) Field-theoretic simulations of polyelectrolyte complexation. *J Polym Sci B Polym Phys* 45:3223–3230.
46. Lee J, Popov YO, Fredrickson GH (2008) Complex coacervation: A field theoretic simulation study of polyelectrolyte complexation. *J Chem Phys* 128:224908.
47. Riggleman RA, Kumar R, Fredrickson GH (2012) Investigation of the interfacial tension of complex coacervates using field-theoretic simulations. *J Chem Phys* 136:024903.
48. Delaney KT, Fredrickson GH (2016) Recent developments in fully fluctuating field-theoretic simulations of polymer melts and solutions. *J Phys Chem B* 120:7615–7634.
49. Wang ZG (2010) Fluctuation in electrolyte solutions: The self energy. *Phys Rev E Stat Nonlinear Soft Matter Phys* 81:021501.
50. Coslovich D, Hansen JP, Kahl G (2011) Ultrasoft primitive model of polyionic solutions: Structure, aggregation, and dynamics. *J Chem Phys* 134:244514.
51. Warren PB, Vlasov A, Anton L, Masters AJ (2013) Screening properties of Gaussian electrolyte models, with application to dissipative particle dynamics. *J Chem Phys*, 138:204907.
52. Parisi G (1983) On complex probabilities. *Phys Lett B* 131:393–395.
53. Klauder JR, Lee S (1992) Improved complex Langevin method for (2+1)-dimensional lattices. *Phys Rev D Part Fields* 45:2101–2104.
54. Plimpton S, Hendrickson B (1996) A new parallel method for molecular dynamics simulation of macromolecular systems. *J Comput Chem* 17:326–337.
55. Kiss PT, Sega M, Baranyai A (2014) Efficient handling of Gaussian charge distributions: An application to polarizable molecular models. *J Chem Theor Comput* 10:5513–5519.
56. Sangster MJL, Dixon M (1976) Interionic potentials in alkali-halides and their use in simulations of molten-salts. *Adv Phys* 25:247–342.
57. Deleeuw SW, Perram JW, Smith ER (1980) Simulation of electrostatic systems in periodic boundary-conditions. I. Lattice sums and dielectric-constants. *Proc R Soc London Ser A* 373:27–56.
58. Liu H, Paddison SJ (2016) Direct calculation of the X-ray structure factor of ionic liquids. *Phys Chem Chem Phys* 18:11000–11007.
59. Sawle L, Ghosh K (2015) A theoretical method to compute sequence dependent configurational properties in charged polymers and proteins. *J Chem Phys* 143:085101.
60. Das RK, Pappu RV (2013) Conformations of intrinsically disordered proteins are influenced by linear sequence distributions of oppositely charged residues. *Proc Natl Acad Sci USA* 110:13392–13397.
61. Perry SL, Sing CE (2015) Prism-based theory of complex coacervation: Excluded volume versus chain correlation. *Macromolecules* 48:5040–5053.
62. Radhakrishna M, et al. (2017) Molecular connectivity and correlation effects on polymer coacervation. *Macromolecules* 50:3030–3037.
63. Lytle TK, Sing CE (2017) Transfer matrix theory of polymer complex coacervation. *Soft Matter* 13:7001–7012.
64. Shen K, Wang ZG (2018) Polyelectrolyte chain structure and solution phase behavior. *Macromolecules* 51:1706–1717.
65. Chang LW, et al. (2017) Sequence and entropy-based control of complex coacervates. *Nat Commun* 8:1273.